



1 **Greenhouse gas effects on the solar cycle response of water vapour and noctilucent**
2 **clouds**

3 Ashique Vellalassery¹, Gerd Baumgarten¹, Mykhaylo Grygalashvyly¹, and Franz-Josef

4 Lübken¹

5 ¹Leibniz Institute of Atmospheric Physics at the University of Rostock, Schloßstraße 6, D-
6 18225 Kühlungsborn, Germany

7 *Correspondence to:* Ashique Vellalassery (ashique@iap-kborn.de)

8

9 **Abstract**

10

11 The response of water vapour (H₂O) and noctilucent clouds (NLCs) to the solar cycle are
12 studied using the Leibniz Institute for Middle Atmosphere (LIMA) model and the Mesospheric
13 Ice Microphysics And tranSport (MIMAS) model. NLCs are sensitive to the solar cycle because
14 their formation depends on background temperature and the H₂O concentration. The solar cycle
15 affects the H₂O concentration in the upper mesosphere mainly in two ways: directly through
16 the photolysis and, in time and place of NLCs formation, indirectly through temperature
17 changes. We found that H₂O concentration correlate positively with the temperature changes
18 due to the solar cycle at altitudes above about 82 km, where NLCs form. The photolysis effect
19 leads to an anti-correlation of H₂O concentration and solar Lyman- α radiation, which gets even
20 more pronounced at altitudes below ~83 km when NLCs are present. We studied the H₂O
21 response to Lyman- α variability for the period 1992 to 2018, including the two most recent
22 solar cycles. The amplitude of Lyman- α variation decreased by about 40% in the period 2005
23 to 2018 compared to the preceding solar cycle, resulting in a lower H₂O response in the late
24 period. We investigated the effect of increasing greenhouse gases (GHGs) on the H₂O response
25 throughout the solar cycle by performing model runs with and without increases in carbon
26 dioxide (CO₂) and methane (CH₄). The increase of methane and carbon dioxide amplify the



27 response of water vapour to the solar variability. The solar cycle response is reduced in the late
28 solar cycle due to a smaller amplitude of Lyman- α variability in the second period. Applying
29 the geometry of satellite observations, we find a missing response when averaging over altitudes
30 of 80 to 85 km, where H₂O has a positive and a negative response (depending on altitude) which
31 largely cancel out. One main finding is that during NLCs the solar cycle response of H₂O
32 strongly depends on altitude. A negative correlation between H₂O and Lyman- α is found in the
33 NLC sublimation zone below an altitude of about 83 km, but a positive response is present at
34 the altitudes above 83 km where NLCs form.

35

36 **1. Introduction**

37

38 The 11-year solar cycle significantly influences the upper atmosphere's temperature and water
39 vapour (H₂O) concentration. H₂O is one of the essential minor constituents in the mesosphere
40 as it is the primary source of chemically active hydrogen radicals, influencing the chemistry of
41 all other chemically active minor constituents (Brasseur and Solomon, 2005, Hartogh et al.,
42 2010). H₂O concentration plays an essential role in the noctilucent cloud's (NLC) formation.
43 NLCs are located at about 83 km altitude, consist of water ice particles, and owe their existence
44 to the cold summer mesopause region (~130K) at mid and high latitudes. NLCs, also called
45 polar mesospheric clouds, are formed in an environment where small changes in background
46 H₂O and temperature can lead to significant changes in NLC properties (e.g., Thomas, 1996;
47 DeLand et al., 2006; Shettle et al., 2009, Lübken et al., 2009).

48 In comparison to the lower atmosphere, little is known about the upper mesosphere/lower
49 thermosphere (MLT, 75-110 km) due to a lack of observations at these altitudes. NLCs have
50 been proposed as indicators of trends (Thomas & Olivero, 2001). Studying NLC properties
51 provide insight in phenomena occurring at the altitude of NLC. The 11-year solar cycle has
52 been considered to cause quasi decadal oscillation observed in NLCs (DeLand et al., 2003).



53 NLCs are predicted to decrease during solar maximum due to increased heating and photolysis
54 of H₂O (Garcia, 1989). However, some recent studies strongly suggest that the response of
55 NLCs to the solar cycle has been absent from 2002 to the present (Fiedler et al., 2011; DeLand
56 & Thomas, 2015; Hervig et al., 2016; Siskind et al., 2013). Hervig et al. (2019), using satellite
57 observations, found that NLC had a clear anti-correlation with the solar cycle before 2002, and
58 that response has been absent in recent years. The leading cause of this absence appears to be
59 the suppression of the solar cycle response of H₂O. Lyman- α (Ly α) radiation is the primary
60 cause of H₂O photolysis and varies by a factor of two between solar minimum and maximum
61 (Woods et al., 2000). Understanding the effects of the solar cycle on H₂O is more complicated
62 at NLC altitudes because of the interaction between NLCs and background H₂O.

63 NLC growth leads to dehydration at higher altitudes (83-89 km) as ice particles are formed by
64 consuming background H₂O, and sublimation of ice particles leads to hydration at lower
65 altitudes as H₂O is released here (about 78-83 km) (Lübken et al., 2009, Hervig et al., 2003).
66 Investigating the effects of NLC on the background H₂O requires an estimate of the H₂O profile
67 without NLCs. Investigations using satellite observations are limited due to uncertainty in the
68 inferred background H₂O without NLC and vertical resolutions in the order of a few 100~m.
69 Therefore, using satellite observations to study H₂O at NLC altitudes could yield misleading
70 results due to biases in the estimated H₂O profiles without NLC (Hervig et al., 2015). Hervig
71 et al. (2015) suggest that in future studies, one approach to investigate the effects of NLC on
72 H₂O would be to use a detailed microphysical NLC model. NLC model simulations are
73 performed with and without microphysics using the same background conditions, resulting in
74 a H₂O profile without NLC. This allows us to investigate how NLC formation changes the H₂O
75 background profile in detail.

76 We compare the model result to satellite observations published by Hervig et al. (2019) to
77 investigate the mechanism behind the solar cycle response of NLC and H₂O. We also focus on
78 the missing solar cycle response of H₂O during recent years. This paper aims to answer a



79 number of questions: How does the formation of NLCs affect the H₂O profile and the variation
80 of water vapour with the solar cycle? How do the solar cycle-induced temperature and
81 photolysis changes affect the H₂O response? Why is the response of water vapour to solar cycle
82 nearly absent in satellite observations after 2005 (Hervig et al., 2019)? Our study is focused on
83 the core NLC period, i.e., July at 68±5°N. The following section describes the modelling
84 framework of this study and discusses the various model simulations performed. The third
85 section discusses the mechanisms behind the solar cycle H₂O response, such as the separation
86 of the solar cycle-induced temperature and photolysis effects on H₂O. Sections four and five
87 explore the possible reasons behind the missing solar cycle response. Concluding remarks and
88 a summary are given in the last section.

89

90 **2. Model description and numerical experiments**

91

92 **2.1. Model**

93

94 The modelling framework used in this study consists mainly of two components: the Leibniz
95 Institute Middle Atmosphere (LIMA) model and the Mesospheric Ice Microphysics And
96 tranSport (MIMAS) model (see Fig. 1). LIMA is a non-linear, global, 3D Eulerian grid-point
97 model reaching from the troposphere to the lower thermosphere, which calculates winds and
98 temperature and is well described in a number of papers (Berger, 2008; Lübken et al., 2013).
99 The LIMA model in this study is nudged to reanalysis data NOAA-CIRES (National Oceanic
100 and Atmospheric Administration-Cooperative Institute for Research in Environmental Sciences
101 20CR; Compo et al., 2011) in the lower atmosphere. The resulting winds and temperatures in
102 the mesosphere and lower thermosphere (MLT) are then used in MIMAS. The MIMAS model
103 run was performed for all years with background wind conditions and gravity wave forcing
104 from a representative year (1976).



105 MIMAS is a 3D Lagrangian transport model specifically designed for modelling ice particles
106 in MLT region (Berger and Lübken, 2015). MIMAS calculate NLC parameters from 10 May
107 to 31 August, and it is constrained from mid-latitudes to high latitudes (37°-90°N) with a
108 horizontal grid resolution of 1° in latitude and 3° in longitude and a vertical resolution of 100
109 m from 77.8 to 94.1 km (163 levels). In this study, the dynamics calculated by LIMA, solar
110 $\text{Ly}\alpha$, and the initial H_2O distribution are the input for MIMAS as sketched in Figure 1. Two
111 effects determine the mixing ratio of H_2O in the mesosphere: (i) transport of H_2O from lower
112 altitudes and (ii) oxidation of methane (CH_4). The oxidation of each CH_4 molecule produces
113 two H_2O molecules. Methane is nearly completely converted to H_2O in the mesosphere by
114 photochemical processes (e.g., Lübken et al., 2018). MIMAS assumes that the H_2O mixing ratio
115 transported from lower altitudes is constant. Therefore, H_2O concentration varies only
116 according to CH_4 concentration (Lübken et al., 2018). Mesospheric H_2O in MIMAS is
117 transported by background winds, dispersed by turbulent diffusion, and reduced by photolysis.
118 MIMAS makes use of 40 million dust particles, which can act as condensation nuclei. These
119 are then coated with ice in H_2O supersaturated regions and transported according to three-
120 dimensional and time-dependent background winds, eddy diffusion, and sedimentation. In
121 MIMAS, standard microphysical processes such as the Kelvin effect determine the nucleation
122 and growth of ice particles (Berger & Lübken, 2015; Gadsden & Schröder, 1989). For the
123 comparison with satellites, we used model run A, which includes CO_2 and CH_4 variations
124 (Lübken et al., 2018; Lübken et al., 2021). We performed MIMAS model simulations with ice
125 formation turned off and on respectively to investigate the effects of ice formation on
126 background H_2O . In both runs, the background conditions and model inputs are the same. The
127 main outputs of the model are the microphysical properties of the NLC ice particles, such as
128 radius, backscatter value, and the number density of the ice/dust particles. More detailed
129 descriptions of the MIMAS model and its precursors are available in the literature (Berger and

Fig. 1



130 von Zahn, 2002; Berger, 2008; Berger and Lübken, 2011; Lübken et al., 2018; Lübken et al.,
131 2021).

132

133 **2.2. Model simulations**

134

135 LIMA and MIMAS use daily Ly α fluxes as a proxy for solar activity from 1961 to 2019. Ly α
136 (and other bands) variations in LIMA cause atmospheric temperature variations, while Ly α
137 variations in MIMAS cause photolysis of H₂O. In LIMA, variation of other bands, namely,
138 Chappius band, Huggins band, Hartley band, Schumann-Runge band, and both Schumann-
139 Runge continuums are parametrised following the Hamburg Model of the Neutral and Ionized
140 Atmosphere (Schmidt et al., 2006) according to Lean et al. (1997). Therefore, it is possible to
141 study the effects of solar cycle on H₂O due to temperature changes and photolysis separately
142 by performing model simulations with constant and varying Ly α in MIMAS and LIMA. We
143 conducted four model runs, as described in Table 1. We also performed LIMA model
144 simulations with constant CO₂ for runs E, F, and G to filter out their effects on temperature
145 changes. For these runs we use a constant CH₄ concentration in MIMAS to avoid its influence
146 on the H₂O profile.

147 In LIMA, the mixing ratios of CO₂ (28-150 km) vary as function of time (years), while all other
148 trace gases are kept constant. An increase in CO₂ leads to a decrease in temperature in the
149 stratosphere mainly due to enhanced cooling by CO₂ (e.g., Roble and Dickinson, 1989; Garcia
150 et al., 2007; Berger & Lübken, 2011; Marsh et al., 2013; Lübken et al., 2013). At NLC altitudes,
151 this cooling leads to an altitude decrease of pressure levels, referred to as the ‘shrinking effect’
152 (Lübken et al., 2009). For LIMA we use the long-term increase of CO₂ concentration according
153 to observations at Mauna Loa (19°N, 155°W).

154 This study focuses mainly on the recent two solar cycles from 1992 to 2018. Figure 2 shows
155 the time series of Ly α , CO₂, and CH₄ for 1992-2018. The corresponding values of Ly α , CH₄,

Fig. 2



156 and CO₂ for the years considered for this study are highlighted. We classify 1992-2005 as period
157 1 (“early”) and 2005-2018 as period 2 (“late”). Satellite observations of H₂O showed a clear
158 anti-correlation with the solar cycle in the early period, which was absent in the late period
159 (Hervig et al. 2019). To investigate this, we first examined the early period solar minimum
160 (1997) and maximum (2002) in more detail. The solar cycle affects the H₂O concentration in
161 two main ways. (i) through the photolysis of H₂O by Ly α , and (ii) through the temperature
162 effect. We distinguish these effects by performing model simulations with different background
163 conditions (see Table 1). Namely in section 3.3, we discuss the individual role of solar cycle-
164 induced photolysis and temperature change on the H₂O-solar cycle response. Figure 2 shows
165 that the intensity of Ly α radiation during the late period has decreased compared to the early
166 period, and the concentrations of increased greenhouse gases (GHGs) have increased in the late
167 period. The effects of reduced Ly α intensity and increased greenhouse gas (GHG)
168 concentration on long-term H₂O-solar cycle response are discussed in section 4.

169

170 3. Results and Discussions

171

172 3.1. Solar cycle response in ice water content (IWC)

173

174 To determine if the model agrees with satellite observations, we compared the ice water content
175 (IWC) anomaly from the model with the satellite observations (see Fig. 3). IWC anomalies are
176 calculated as follows:

$$177 \quad IWC_{anom} = 100\% \cdot \frac{\overline{IWC_{July}} - \overline{IWC_{1981-2018}}}{\overline{IWC_{1981-2018}}}, \quad (1)$$

178 Where $\overline{IWC_{July}}$ represent monthly zonal averages at 68°N, and $\overline{IWC_{1981-2018}}$ are the averages
179 of $\overline{IWC_{July}}$ over the years 1981-2018. The IWC anomaly for satellite measurements are from
180 the Solar Backscatter Ultraviolet (SBUV), Halogen Occultation Experiment (HALOE), Cloud

Fig. 3



181 Imaging and Particle Size (CIPS), and Solar Occultation For Ice Experiment (SOFIE)
182 instruments. The time series of SBUV and HALOE data as shown in Figure 3 represent three
183 years sliding averaged values. For more details on the satellite datasets, see Hervig et al. (2019).
184 For this comparison, we used the MIMAS run A, in which the simulations are performed with
185 increasing concentrations of CO₂ and CH₄. For the comparison, we applied the same calculation
186 method to our model data as Hervig et al. (2019) did on satellite observations, namely, we used
187 a threshold of 50 g/km³ for integrated water content because the PMC detection threshold for
188 SBUV is 50 g/km³ (DeLand and Thomas, 2015, 2019).

189 We find an anti-correlation between MIMAS IWC anomaly and Ly α flux throughout the entire
190 period (1981-2018), with a weaker response in the late period. In satellite observations, SBUV
191 measurements also show an anti-correlation with Ly α flux until 2005, after which the response
192 becomes weaker in agreement with MIMAS. The magnitude of the solar cycle IWC anomaly
193 in SBUV and HALOE is of the same order as the IWC anomaly in MIMAS. The IWC anomalies
194 of CIPS and SOFIE do not show a clear response to the solar cycle. We notice that the year-to-
195 year IWC variation in CIPS and SOFIE is larger than the IWC modulation during a solar cycle.
196 IWC anomalies of SBUV and HALOE correlate well with MIMAS IWC anomalies before 2005
197 and progressively weaken afterwards. Lübken et al. (2009) found a good agreement between
198 NLC parameters calculated by MIMAS and satellite observations. The general agreement
199 between the main characteristics and trends of the ice layers in MIMAS and the observations
200 suggests that the microphysical and photochemical processes in MIMAS cover the main
201 processes relevant to NLC formation (Lübken et al., 2009).

202

203 **3.2. Effect of NLC on water vapour (H₂O)**

204

205 We calculated the zonal mean monthly averaged vertical profiles of H₂O and temperature to
206 investigate the impact of NLC formation on the H₂O profile. Figure 4 shows the vertical H₂O

Fig. 4



207 profile averaged for July at 68°N latitude and given on pressure altitudes $z_p = H_p \ln(p_0/p)$.
208 Where p is the pressure of the model level, p_0 is the pressure at the surface and $H_p = 7$ km is
209 the pressure scale height. This figure illustrates the effect of NLC formation on the background
210 profile of water vapour since the H₂O profile with NLC differs from that without NLC. In the
211 presence of NLC there is a reduction in water vapour mixing ratio (dehydration) between 83-
212 90 km, i.e. in the region where the saturation ratio of water vapour is larger than one. An
213 enhancement in water vapour (hydration) is observed at altitudes between 79-83 km, where the
214 saturation ratio of water vapour is smaller than one. An environment with a water vapour
215 saturation ratio larger than one is supersaturated, meaning ice particles can grow under these
216 conditions whereas a saturation ratio lower than one leads to ice sublimation. The degree of
217 saturation depends on the background atmosphere's H₂O concentration, and temperature. Ice
218 particles formation starts at higher altitudes, where the temperature is the lowest, and then they
219 sediment downward. During sedimentation, the ice particles grow by consuming H₂O from the
220 surrounding background, which decreases background H₂O concentration. Then they approach
221 a region with a saturation ratio smaller than one, where they sublimate, releasing the water
222 vapour. This is the so-called freeze-drying effect well discussed in a number of papers (Hervig
223 et al., 2003; Lübken et al., 2009; Bardeen et al., 2010). The results in Figure 4 also indicate that
224 the effects of NLC on H₂O are not present below ~79 km and above ~97 km. This is because
225 the photochemical lifetime of water vapour below ~79 km becomes larger than dynamical
226 characteristic times, and distributions of water vapour become dynamically determined. Above
227 97 km, the saturation ratio of water vapour is smaller than one; consequently, there is no NLC
228 formation and consequently no effect on water vapour.

229

230 **3.3. Effect of solar cycle-induced temperature and photolysis changes on water vapour**
231 **(H₂O)**



232

233 We investigate the temperature change between the solar minimum (1997) and maximum
234 (2002) due to solar irradiance variation and how these change affect the H₂O profile. Different
235 model runs performed for this study are summarized in Table 1. The differences (solar
236 maximum - solar minimum) for H₂O and temperature profiles are shown in Figure 5 for three
237 model runs, namely E, F, and G. In run E, the solar cycle-induced temperature change and
238 photolysis influences H₂O concentration. In run F, only the temperature change caused by the
239 solar cycle affects the H₂O concentration, while in run G, only the photolysis caused by the
240 solar cycle affects the H₂O concentration (see Table 1). All of these runs are performed with
241 constant CO₂ and CH₄ concentrations to avoid the effects of increasing GHG concentrations on
242 temperature and H₂O profiles.

243 In model run F, Ly α is held constant in MIMAS, so the photolysis of H₂O is constant during
244 the solar cycle. However, Ly α (and other bands) varies in the LIMA model, so the background
245 temperature varies with the solar cycle. Therefore, the change in the H₂O profile during the
246 solar cycle is only due to the influence of the solar cycle on temperature and sequentially on
247 microphysical processes. Figure 5a shows that the temperature increases during solar maximum
248 compared to solar minimum through the entire altitude range (79-97 km). The difference of
249 temperature amounts to ~0.5-1.7 K with maximum values at ~95 km. During solar maximum,
250 increased solar irradiance leads to greater absorption of solar radiation in the MLT region by
251 molecular oxygen and water vapour, which heats the background atmosphere. Temperature
252 differences decrease as altitude decreases because the intensity of solar radiation decreases due
253 to atmospheric absorption. The solar cycle effect in the H₂O profile with NLC (blue line) differs
254 significantly from that without NLC (yellow line). Without NLC, the H₂O profile difference is
255 nearly zero at all altitudes, indicating that the temperature changes do not significantly affect
256 the background H₂O profile in the absence of NLC. With NLC, the H₂O profile difference is
257 positive in the altitude range of 82-87 km and slightly negative in the range from 79 to 82 km.

Fig. 5a



258 The atmosphere is warmer during solar maximum; therefore, the ice formation rate is lower
259 during solar maximum. When the ice formation rate decreases, the amount of water vapour
260 consumed from the background decreases; hence, more H₂O is left in the background during
261 solar maximum compared to solar minimum, resulting in a slightly positive response at NLC
262 forming altitudes above 83 km. Below that altitude, the slightly negative response is due to
263 reduced ice formation in the nucleation region during solar maximum, which decreases H₂O
264 released at ice sublimation altitudes. The positive difference peak at ~83 km is located near the
265 bottom of the H₂O-saturated zone. Ice formation/sublimation is more sensitive to an increase
266 in background temperature at this zone (where the degree of saturation is close to one) because
267 at these altitudes the background temperature is almost equal to the frost point temperature, so
268 an increase in background temperature critically changes the degree of saturation. The change
269 of the background temperature in a region where it is significantly lower than the frost point
270 temperature is not critical for the degree of saturation. Overall, the temperature variation due to
271 the solar cycle causes a positive H₂O response on the solar cycle at ice-formation altitudes and
272 a slightly negative response at ice-sublimation altitudes.

273 In model run G (Fig. 5b), we consider only the effect of solar cycle-induced Ly α variation on
274 water vapour photolysis. The background temperature is held constant. Photolysis of H₂O by
275 Ly α radiation molecules mainly leads to atomic hydrogen (H) and hydroxyl (OH) in the upper
276 atmosphere (~90 %) and with less extent to O(¹D) with molecular hydrogen (~10 %). The
277 photolysis rate is higher during solar maximum due to the increased Ly α flux caused by the
278 increased solar activity. Without NLC, the difference in the H₂O profile is negative at all
279 altitudes (yellow line), indicating that the background H₂O is reduced during solar maximum
280 due to increased photolysis. Figure 5b shows that the negative response peaks at an altitude of
281 ~87.5 km. The solar cycle effect on the photolysis of H₂O decreases above 87.5 km because the
282 water vapour mixing ratio decreases with increasing altitude. The solar cycle variation of the
283 photolysis effect decreases below 87.5 km because the solar Ly α radiation intensity decreases.

Fig. 5b



284 With NLC (blue line), the H₂O difference between the solar maximum and the solar minimum
285 is essentially negative at ice sublimation altitudes (below ~83 km) and negligible at higher
286 altitudes (above ~85 km). This is due to the redistribution of the H₂O profile during NLC
287 formation (“freeze-drying”). During solar maximum, the background H₂O concentration
288 available for ice formation is reduced due to enhanced photolysis. The lower H₂O availability
289 during solar maximum results in lower ice formation and, thus, lower H₂O release during
290 sublimation, leading to lower hydration in the sublimation zone. For this reason, the solar cycle
291 variation of the photolysis effect is more pronounced at sublimation altitudes. Above 85 km,
292 the effect of photolysis, in the case with NLC, is minimal because of the lower availability of
293 H₂O due to dehydration by NLC.

294 Figure 5c shows a combination of both effects, namely the solar cycle-induced temperature
295 change and photolysis effects on H₂O. Without NLC (yellow line), the H₂O profile shows a
296 negative response at all altitudes, peaking at ~87.5 km similar to run G (Fig. 5b, yellow line).
297 We found that the variation of temperature has an almost negligible effect on the H₂O in the
298 absence of NLC (see Fig. 5a, yellow line), so the negative response of water vapour without
299 consideration of microphysical processes (yellow line on Fig. 5c) is mainly caused by the
300 photolysis effect. With NLC (Fig. 5c, blue line), the combined effect of temperature and
301 photolysis has a slightly positive response on water vapour in the ice formation zone (83-89km)
302 and a negative response in the ice sublimation zone (80-83km). The slightly positive response
303 is caused by the temperature modulation, and the negative response is primarily due to the
304 photolysis modulation throughout the solar cycle.

305 The study proves that the water vapour response to the solar cycle is affected by the re-
306 distribution of water in the presence of NLC. There may exist regions with positive correlation
307 of water vapour with Ly α when NLC formation occurs. Without NLC, the water vapour always
308 shows a negative correlation to the solar cycle. When comparing the effects of solar cycle
309 modulations of temperatures and photolysis on H₂O, the photolysis has a stronger effect on

Fig. 5c



310 water vapour, however, the variation of temperature induces a positive correlation of solar
311 irradiance and H₂O.

312

313 4. Increasing greenhouse gases and reducing solar cycle

314

315 This section examines how the increase in GHGs affects the H₂O response to the solar cycle.

316 To distinguish the GHG effects, we compared the model results with increasing CO₂ and CH₄

317 (Run A) to the model run with constant CO₂ and CH₄ (Run E). It is noted already that an

318 increasing CO₂ concentration leads to a cooling of the middle atmosphere, and an increase in

319 CH₄ concentration leads to an increase in H₂O concentration (see Sec.2 for details). In Figure

320 2, the concentration of CO₂ and CH₄ increase during the late period, and at the same time, the

321 peak of the Ly α flux decreases. In order to filter out the effect of reduced Ly α intensity, we

322 calculated the H₂O response profile per unit of Ly α (Δ H₂O / Δ Ly α). Figure 6 shows the result

Fig. 6

323 for the first (1997-2002, blue line) and the second period (2008-2014, orange line) for model

324 runs E (Fig. 6a) and A (Fig. 6b) respectively. These profiles show positive and negative

325 responses depending on altitude. Under the conditions of constant GHGs (run E) the sensitivity

326 of water vapour to Ly α does not change from the early to the late period (Fig. 6a). As expected,

327 for the case of growing methane and carbon dioxide (run A), the sensitivity of water vapour to

328 Ly α increases during the late period (orange line, Fig. 6b) compared to the early period (blue

329 line, Fig. 6b). This is because an increase in CO₂ (and consequently temperature decrease) leads

330 to an intensification of microphysical processes, hence, to the increased freeze-drying. In

331 addition, increasing methane leads to more water vapour in the upper mesosphere, which also

332 leads to an increased water vapour variation with solar cycle.

333 To study the effect of a decreasing Ly α amplitude during the late period (2008-2014), we

334 calculated the ratio of water vapour absolute deviations between solar minimum and solar



335 maximum for the early and late period. The amplitude of Ly α variation is weaker during the
336 late period ($\sim 1.14 \cdot 10^{11}$ [phot.cm $^{-2}$ s $^{-1}$]/solar cycle) compared to the early period ($\sim 1.85 \cdot 10^{11}$
337 [phot.cm $^{-2}$ s $^{-1}$]/solar cycle). The intensity of Ly α during the late period solar maximum is
338 reduced by $\sim 40\%$ compared to the early period. As can be seen from Figure 7a the magnitudes
339 of positive and negative H $_2$ O responses decreased during the late period for model runs with
340 constant GHGs (Run E). In Figure 6a, we found that the H $_2$ O sensitivity to Ly α flux is the same
341 in the early and late periods for the model run with constant GHGs (Run E). Therefore, the
342 reduced response of H $_2$ O during the late period in model run E (Fig. 7a) is only due to the
343 reduced solar Ly α variation. Comparing the late period H $_2$ O response to the solar cycle from
344 model runs with constant GHG (Fig. 7a, orange line) to model runs with increasing GHG (Fig.
345 7b, orange line) suggests that both the positive and negative peak responses are enhanced by
346 increasing GHG concentration.

Fig. 7

347

348 **5. Missing H $_2$ O-solar cycle response**

349

350 A recent study by Hervig et al. (2019) reported a missing response in H $_2$ O concentration on
351 solar cycle after 2005. In Figure 8, we compare our model results of H $_2$ O anomaly with the
352 satellite observations. The H $_2$ O response is averaged over the geometric altitudes of 80-85 km
353 at 68°N. For this comparison, we used MIMAS run A, where the increasing concentration of
354 GHG is considered. The satellite observations are shown in Figure 8 from HALOE, SOFIE,
355 and MLS according to Hervig et al. (2019). HALOE shows a strong negative response to Ly α
356 (-1.7 ppmv/solar cycle) during period 1, but in SOFIE and MLS the response is almost absent
357 ($+0.2$ ppmv/solar cycle) during period 2 (Hervig et al., 2019). For MIMAS, no clear H $_2$ O-solar
358 cycle anti-correlation is noticed in the early period, but it was slightly positive in the late period
359 in agreement with SOFIE and MLS satellite observations. To investigate the H $_2$ O response on

Fig. 8



360 Ly α variation in more detail, we analysed the vertical H₂O response profile at geometric
361 altitudes similar to the satellite observations.

362 Figure 9 shows the vertical profile of H₂O response in geometric altitudes for the model run
363 with constant GHGs (run E, Fig. 9a) and growing GHGs (run A, Fig. 9b). The magnitude of the
364 H₂O response at geometric altitudes (Fig. 9) differs from that at pressure altitudes (Fig.7). This
365 is because the geometric altitude of constant pressure levels is not constant and varies
366 throughout the solar cycle but also with time due to increasing GHG. Therefore, the magnitude
367 of the H₂O response differs when converted from pressure altitudes to geometric altitudes.

Fig. 9

368 We focus on the 80-85 km geometric altitude range (Fig. 9. shaded region). There are positive
369 and negative H₂O response zones within this altitude range similar to Figure 7. We calculated
370 the average H₂O response over 80-85 km altitude range for MIMAS runs A and E is given in
371 Table 2. For the model run with growing GHGs (run A), the H₂O response averaged over an
372 altitude range of 80-85 km changed from -0.01 ppm/solar cycle in the early period to 0.10
373 ppm/solar cycle in the late period (see Table. 2). The H₂O response in the late period becomes
374 slightly positive for run A, consistent with the satellite observations of SOFIE and MLS (see
375 Fig. 8). The vertical profile of H₂O-solarcycle response clearly show that H₂O response to the
376 solar cycle is not completely missing in the late period. The missing response in the MIMAS
377 H₂O as shown in Figure 8 occurred when averaging over the 80-85 km altitude range. Figure 9
378 demonstrates that the H₂O response shows nearly equal positive and negative responses within
379 the 80-85 km altitude range (shaded region). Therefore, averaging the response in this altitude
380 range becomes nearly zero, as the positive and negative responses cancel out each other. When
381 averaging over the altitude range of 80 to 82 km in the early period we receive H₂O response
382 of -0.71ppm/solar cycle and an anti-correlation between H₂O and Ly α . The results clearly
383 shows that the small solar cycle response in MIMAS is a consequence of averaging over an
384 altitude range of 80-85 km. It suggests that averaging H₂O response over an altitude range



385 containing positive and negative responses may not provide a detailed understanding of the
386 H₂O-solar cycle response.

387

388 **6. Conclusions**

389

390 In this study, we used our ice particle model MIMAS along with atmospheric transport model
391 LIMA to investigate the response of H₂O to the solar cycle from 1992-2018. We investigated
392 how NLC formation affects vertical H₂O profiles by running model simulations with and
393 without microphysics. NLC formations are shown to redistribute H₂O profiles by consuming
394 H₂O from the background at ice-forming altitudes (dehydration) and releasing it at ice-
395 sublimating altitudes (hydration) is known as the “freeze-drying” effect. To investigate the
396 missing solar cycle response in satellite observations reported by Hervig et al. (2019), we
397 divided the entire study period into an early (1992-2005) and late (2005-2018) period. We first
398 investigated how the Ly α variation affects the H₂O profile between solar minimum and
399 maximum in the early period. The solar Ly α variation affects the H₂O concentration at NLC
400 altitudes mainly in two ways: through the effect of temperature change and through the effect
401 of photolysis. To distinguish these two effects, we performed additional model simulations with
402 different background conditions (see Table 1). We found that the modulation of water vapour,
403 which comes through the temperature changes with solar cycle, causes a slight positive H₂O
404 response at ice-forming altitudes and a negative response at ice-sublimating altitudes. The solar
405 cycle photolysis effect has only negative responses on the H₂O profile, and this response
406 dominates at ice sublimation altitudes with NLC conditions. Our results for the case of
407 photolysis effect only are supported by previous simulations, which also suggest that freeze-
408 drying significantly reduces the potential effect of Ly α photolysis on H₂O above 82 km, while
409 the effect is enhanced at 80-82 km, where ice particles sublimate (von Zahn et al., 2004, Lübken
410 et al., 2009).



411 To the best of our knowledge, we have for the first time identified a positive response of water
412 vapour to $Ly\alpha$ variation in the MLT region which is due to microphysical processes. It was
413 assumed for a long time that water vapour only anti-correlates with the solar cycle at mesopause
414 altitudes (e.g. Sonnemann and Grygalashvyly, 2005; and references therein). We should note
415 that in the Martian atmosphere, where microphysical processes have a crucial role in water
416 vapour distributions through the entire atmosphere in all seasons (e.g. Shaposhnikov et al.,
417 2018), this effect may be important.

418 We have made a comparison between the model and satellite observations of the H_2O response
419 to the solar cycle, averaged over an altitude range of 80-85 km. The satellite observations from
420 HALOE show a strong anti-correlation to the solar cycle in the early period, but the model
421 shows a very small response in both the early and late periods. The vertical H_2O response
422 profiles from MIMAS show that within the 80-85 km altitude range, the positive and negative
423 responses are almost equal in magnitude and symmetric. Therefore, averaging the response over
424 this altitude range reduces the overall response in model, as positive and negative responses
425 cancel each other out.

426 We also investigated the role of increasing GHG on the H_2O -solar cycle response. From the
427 early to the late period, there are mainly two factors that affect the long-term H_2O solar cycle
428 response: increasing CO_2 and CH_4 concentrations and the lower intensity of the solar cycle (see
429 Figure 2). We found that increasing GHG concentration increased the H_2O response to $Ly\alpha$.
430 The $Ly\alpha$ intensity during the late solar maximum decreased by 40% compared to the early solar
431 maximum. Therefore, the overall response of H_2O to the solar cycle is also decreased in the late
432 period.

433

434 **Appendix**

435 **Data availability.** The data utilized in this manuscript can be downloaded from

436 **Author contributions.** All authors contributed equally to this paper.



437 **Competing interests.**

438 **Acknowledgements.** We acknowledge the Mauna Loa records for CO₂ and CH₄ from
439 <http://www.esrl.noaa.gov/gmd/ccgg/>. This paper is partly supported by the TIMA project of the
440 BMBF research initiative ROMIC.

441

442

443 **References**

444 Berger, U. (2008). Modeling of middle atmosphere dynamics with LIMA. Journal of
445 Atmospheric and Solar-Terrestrial Physics, 70(8–9), 1170–1200.
446 <https://doi.org/10.1016/j.jastp.2008.02.004>

447

448 Berger, U., & Lübken, F. J. (2011). Mesospheric temperature trends at mid-latitudes in summer.
449 Geophysical Research Letters, 38(22). <https://doi.org/10.1029/2011GL049528>

450

451 Berger, U., & Lübken, F. J. (2015). Trends in mesospheric ice layers in the Northern
452 Hemisphere during 1961-2013. Journal of Geophysical Research, 120(21), 11,277-11,298.
453 <https://doi.org/10.1002/2015JD023355>

454

455 Berger, U., & von Zahn, U. (2002). Icy particles in the summer mesopause region: Three-
456 dimensional modeling of their environment and two-dimensional modeling of their transport.
457 Journal of Geophysical Research: Space Physics, 107(A11).
458 <https://doi.org/10.1029/2001JA000316>

459

460 Brasseur, G., and S. Solomon (2005), Aeronomy of the Middle Atmosphere

461



462 Compo, G. P., Whitaker, J. S., Sardeshmukh, P. D., Matsui, N., Allan, R. J., Yin, X., Gleason,
463 B. E., Vose, R. S., Rutledge, G., Bessemoulin, P., BroNnimann, S., Brunet, M., Crouthamel, R.
464 I., Grant, A. N., Groisman, P. Y., Jones, P. D., Kruk, M. C., Kruger, A. C., Marshall, G. J., ...
465 Worley, S. J. (2011). The Twentieth Century Reanalysis Project. In Quarterly Journal of the
466 Royal Meteorological Society (Vol. 137, Issue 654, pp. 1–28). John Wiley and Sons Ltd.
467 <https://doi.org/10.1002/qj.776>
468
469 DeLand, M. T., & Thomas, G. E. (2015). Updated PMC trends derived from SBUV data.
470 Journal of Geophysical Research, 120(5), 2140–2166. <https://doi.org/10.1002/2014JD022253>
471
472 DeLand, M. T., & Thomas, G. E. (2019). Evaluation of Space Traffic Effects in SBUV Polar
473 Mesospheric Cloud Data. Journal of geophysical research. Atmospheres JGR, 124(7), 4203–
474 4221. <https://doi.org/10.1029/2018JD029756>
475
476 DeLand, M. T., Shettle, E. P., Thomas, G. E., & Olivero, J. J. (2006). A quarter-century of
477 satellite polar mesospheric cloud observations. Journal of Atmospheric and Solar-Terrestrial
478 Physics, 68(1), 9–29. <https://doi.org/10.1016/J.JASTP.2005.08.003>
479
480 DeLand, M. T., Shettle, E. P., Thomas, G. E., & Olivero, J. J. (2003). Solar backscattered
481 ultraviolet (SBUV) observations of polar mesospheric clouds (PMCs) over two solar cycles.
482 Journal of Geophysical Research: Atmospheres, 108(8). <https://doi.org/10.1029/2002jd002398>
483
484 Fiedler, J., Baumgarten, G., Berger, U., Hoffmann, P., Kaifler, N., & Lübken, F. J. (2011). NLC
485 and the background atmosphere above ALOMAR. Atmospheric Chemistry and Physics,
486 11(12), 5701–5717. <https://doi.org/10.5194/acp-11-5701-2011>
487



488 Gadsden, M., & Schröder, W. (1989). Noctilucent Clouds. Noctilucent Clouds, 1–
489 12. doi:10.1007/978-3-642-48626-5_1

490

491 Garcia, R. R., Marsh, D. R., Kinnison, D. E., Boville, B. A., & Sassi, F. (2007). Simulation of
492 secular trends in the middle atmosphere, 1950-2003. Journal of Geophysical Research
493 Atmospheres, 112(9). <https://doi.org/10.1029/2006JD007485>

494

495 Garcia, R. R. (1989). Dynamics, Radiation, and Photochemistry in the Mesosphere’
496 Implications for the Formation of Noctilucent Clouds. In JOURNAL OF GEOPHYSICAL
497 RESEARCH (Vol. 94, Issue D12).

498

499 Hartogh, P., Sonnemann, G. R., Grygalashvyly, M., Song, L., Berger, U., & Lübken, F.-J.
500 (2010). H₂O measurements at ALOMAR over a solar cycle compared with model calculations
501 by LIMA. Journal of Geophysical Research, 115. <https://doi.org/10.1029/2009jd012364>

502

503 Hervig, M., McHugh, M., and Summers, M. E. (2003), Water vapor enhancement in the polar
504 summer mesosphere and its relationship to polar mesospheric clouds, Geophys. Res. Lett., 30,
505 2041, doi:10.1029/2003GL018089, 20.

506

507 Hervig, M. E., Berger, U., & Siskind, D. E. (2016). Decadal variability in PMCs and
508 implications for changing temperature and H₂O in the upper mesosphere. Journal of
509 Geophysical Research, 121(5), 2383–2392. <https://doi.org/10.1002/2015JD024439>

510

511 Hervig, M. E., Siskind, D. E., Bailey, S. M., & Russell, J. M. (2015). The influence of PMCs
512 on water vapor and drivers behind PMC variability from SOFIE observations. Journal of



513 Atmospheric and Solar-Terrestrial Physics, 132, 124–134.

514 <https://doi.org/10.1016/j.jastp.2015.07.010>

515

516 Hervig, M. E., Siskind, D. E., Bailey, S. M., Merkel, A. W., DeLand, M. T., & Russell, J. M.

517 (2019). The Missing Solar Cycle Response of the Polar Summer Mesosphere. *Geophysical*

518 *Research Letters*, 46(16), 10132–10139. <https://doi.org/10.1029/2019GL083485>

519

520 Lean, J. L., Rottman, G. J., Kyle, H. L., Woods, T. N., Hickey, J. R., and Puga, L. C.: Detection

521 and parameterization of variations in solar mid- and near-ultraviolet radiation (200–400 nm), *J.*

522 *Geophys. Res.*, 102, 29939–29956, doi:10.1029/95GL03093, 1997.

523

524 Lübken, F. J., Baumgarten, G., & Berger, U. (2021). Long term trends of mesospheric ice layers:

525 A model study. *Journal of Atmospheric and Solar-Terrestrial Physics*, 214.

526 <https://doi.org/10.1016/j.jastp.2020.105378>

527

528 Lübken, F. J., Berger, U., & Baumgarten, G. (2009). Stratospheric and solar cycle effects on

529 long-term variability of mesospheric ice clouds. *Journal of Geophysical Research Atmospheres*,

530 114(21). <https://doi.org/10.1029/2009JD012377>

531

532 Lübken, F. J., Berger, U., & Baumgarten, G. (2013). Temperature trends in the midlatitude

533 summer mesosphere. *Journal of Geophysical Research Atmospheres*, 118(24), 13,347–13,360.

534 <https://doi.org/10.1002/2013JD020576>

535

536 Lübken, F. J., Berger, U., & Baumgarten, G. (2018). On the Anthropogenic Impact on Long-

537 Term Evolution of Noctilucent Clouds. *Geophysical Research Letters*, 45(13), 6681–6689.

538 <https://doi.org/10.1029/2018GL077719>



539

540 Marsh, D. R., Mills, M. J., Kinnison, D. E., Lamarque, J. F., Calvo, N., & Polvani, L. M. (2013).
541 Climate change from 1850 to 2005 simulated in CESM1(WACCM). *Journal of Climate*, 26(19),
542 7372–7391. <https://doi.org/10.1175/JCLI-D-12-00558.1>

543

544 Medvedev, A. S., & Klaassen, G. P. (2000). Parameterization of gravity wave momentum
545 deposition based on nonlinear wave interactions: basic formulation and sensitivity tests. *Journal*
546 *of Atmospheric and Solar-Terrestrial Physics*, 62. www.elsevier.nl/locate/jastp

547

548 Roble, R. and Dickinson, R. (1989) How Will Changes in Carbon Dioxide and Methane Modify
549 the Mean Structure of the Mesosphere and Thermosphere? *Geophysical Research Letters*, 16,
550 1441-1444. <https://doi.org/10.1029/GL016i012p01441>

551

552 Sonnemann, G. R., & Grygalashvyly, M. (2005). Solar influence on mesospheric water vapor
553 with impact on NLCs. *Journal of Atmospheric and Solar-Terrestrial Physics*, 67(1–2), 177–
554 190. <https://doi.org/10.1016/j.jastp.2004.07.026>

555

556 Shaposhnikov, D. S., Rodin, A. V., Medvedev, A. S., Fedorova, A. A., Kuroda, T., & Hartogh,
557 P. (2018). Modeling the hydrological cycle in the atmosphere of Mars: Influence of a bimodal
558 size distribution of aerosol nucleation particles. *Journal of Geophysical Research: Planets*, 123,
559 508–526. <https://doi.org/10.1002/2017JE005384>

560

561 Shettle, E. P., DeLand, M. T., Thomas, G. E., & Olivero, J. J. (2009). Long term variations in
562 the frequency of polar mesospheric clouds in the Northern Hemisphere from SBUV.
563 *Geophysical Research Letters*, 36(2). <https://doi.org/10.1029/2008GL036048>

564



565 Schmidt, H., G. P. Brasseur, M. Charron, E. Manzini, M. A. Giorgetta, T. Diehl, V. I. Fomichev,
566 D. Kinnison, D. Marsh, and S. Walters, (2006). The HAMMONIA chemistry climate model:
567 Sensitivity of the mesopause region to the 11-year solar cycle and CO₂ doubling. *J. Climate*,
568 19, 3903—3931.

569

570 Siskind, D. E., Stevens, M. H., Hervig, M. E., & Randall, C. E. (2013). Recent observations of
571 high mass density polar mesospheric clouds: A link to space traffic? *Geophysical Research*
572 *Letters*, 40(11), 2813–2817. <https://doi.org/10.1002/grl.50540>

573

574 Thomas, G. E. (1996). IS THE POLAR MESOSPHERE THE MINER'S CANARY OF
575 GLOBAL CHANGE? In *Adv. Space Res* (Vol. 18, Issue 3).

576

577 Thomas, G. E., & Olivero, J. (2001). Noctilucent clouds as possible indicators of global change
578 in the mesosphere. *Advances in Space Research*, 28(7), 937–946.
579 [https://doi.org/10.1016/S0273-1177\(01\)80021-1](https://doi.org/10.1016/S0273-1177(01)80021-1)

580

581 von Zahn, U., & Berger, U. (2003). Persistent ice cloud in the midsummer upper mesosphere
582 at high latitudes: Three-dimensional modeling and cloud interactions with ambient H₂O.
583 *Journal of Geophysical Research: Atmospheres*, 108(8). <https://doi.org/10.1029/2002jd002409>

584

585 von Zahn, U., Baumgarten, G., Berger, U., Fiedler, J., & Hartogh, P. (2004). Atmospheric
586 Chemistry and Physics Noctilucent clouds and the mesospheric water vapour: the past decade.
587 In *Atmos. Chem. Phys* (Vol. 4). www.atmos-chem-phys.org/acp/4/2449/

588

589 Woods, T. N., Tobiska, W. K., Rottman, G. J., & Worden, J. R. (2000). Improved solar Lyman
590 α irradiance modeling from 1947 through 1999 based on UARS observations. In *Journal of*



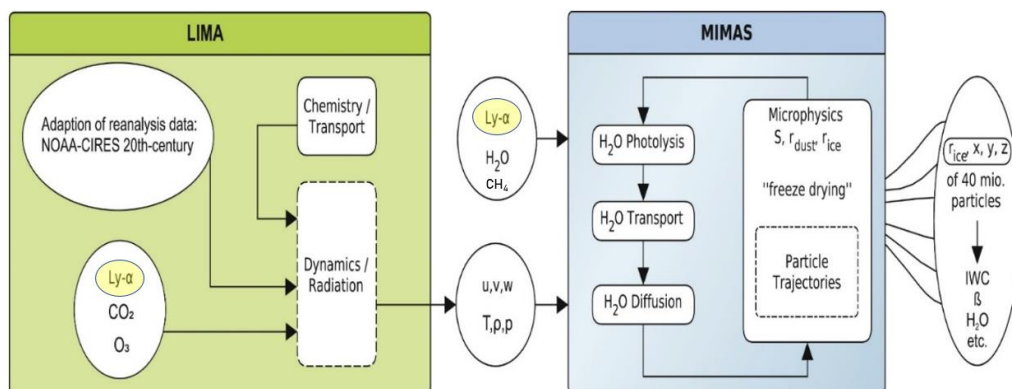
591 Geophysical Research: Space Physics (Vol. 105, Issue A12, pp. 27195–27215). Blackwell
592 Publishing Ltd. <https://doi.org/10.1029/2000ja000051>
593



594 **Figures**

595

596 Figure 1. Sketch of the LIMA (green) and MIMAS (blue) models (from Lübken et al., 2021)



597

598

599

600

601

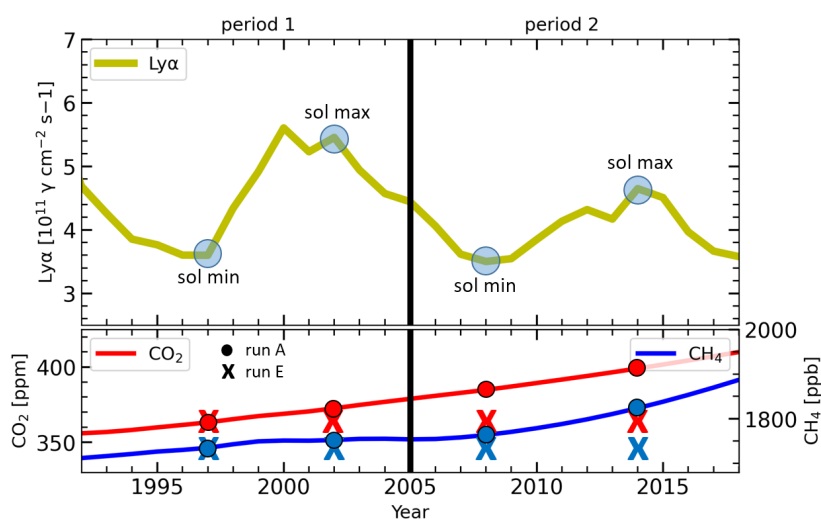
602

603

604



605 Figure 2. Time series of solar $\text{Ly}\alpha$, CO_2 , and CH_4 for 1992-2018. The corresponding $\text{Ly}\alpha$,
606 CO_2 , and CH_4 values for the solar cycle maximum and minimum years used for this study are
607 marked. The CO_2 and CH_4 values for run A are represented with dots, and for run E with
608 crosses. The study period is divided into period 1 as early (1992-2005) and period 2 as late
609 (2005-2018).

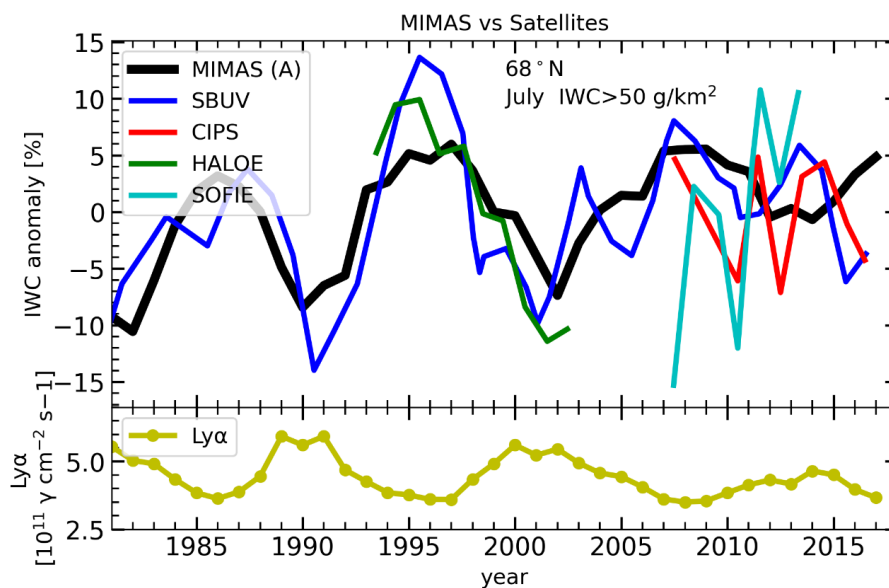


610

611



612 Figure 3. Time series of July mean IWC anomalies at 68°N from model and satellites based on
613 Hervig et al., (2019). Anomalies for each data set are calculated as the difference from their
614 long-term mean. To reduce year to year variability, the time series of SBUV and HALOE are
615 smoothed using the sliding average method of window size 3. Ly α -solar cycle modulation is
616 shown in the bottom panel.

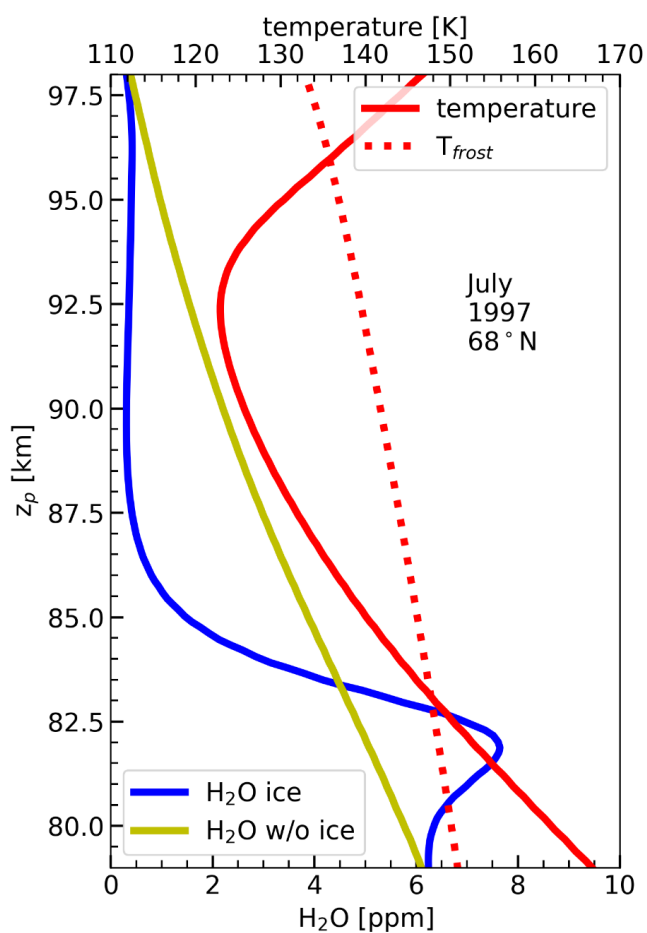


617

618



619 Figure 4. Zonally and monthly averaged H₂O and temperature profile for July at 68°N from
620 MIMAS with and without NLCs. The red dotted line represents frost point temperature. The
621 blue lines show the background H₂O concentration with NLC, and the yellow lines show the
622 H₂O concentration without NLC.

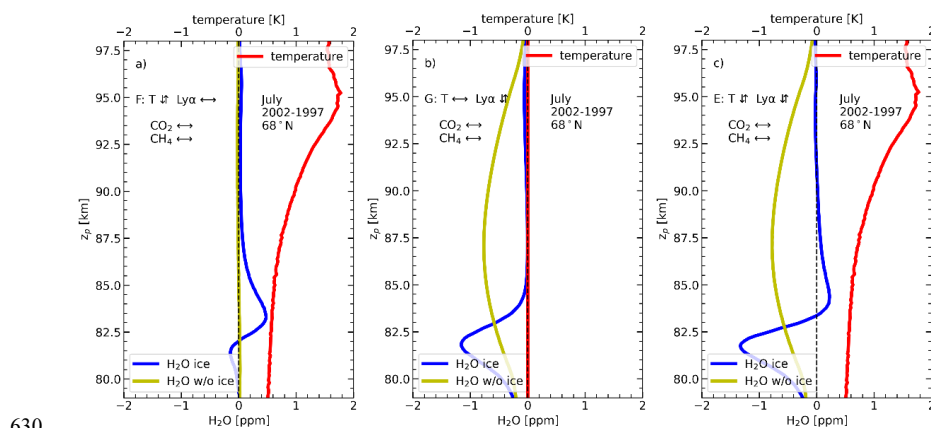


623

624



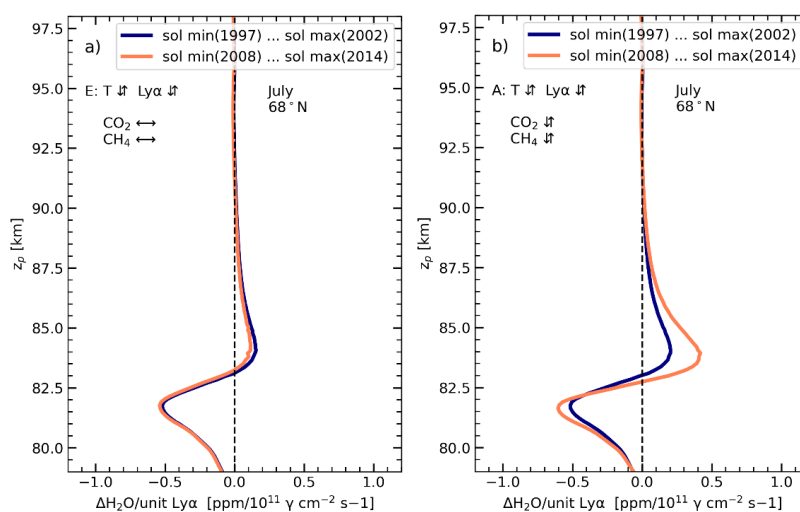
625 Figure 5. The difference in profiles between solar maximum (2002) and minimum (1997) for
626 July mean H₂O and temperatures. The blue and yellow lines represent NLC and non-NLC
627 conditions. In all cases, CO₂ and CH₄ values are constant corresponding to 1997. (a) Run F:
628 only temperature change effects on H₂O, (b) Run G: only Photolysis change effect on H₂O, (c)
629 Run E: both temperature change and photolysis change effects on H₂O



630



631 Figure 6. H₂O-response per unit Ly α variations in July at 68°N during the years between solar
632 minimum and maximum in the early (1997 to 2002) and late (2008 to 2014) periods. (a)
633 MIMAS model run E with constant CO₂ and CH₄, (b) MIMAS model run A with varying CO₂
634 and CH₄.



635

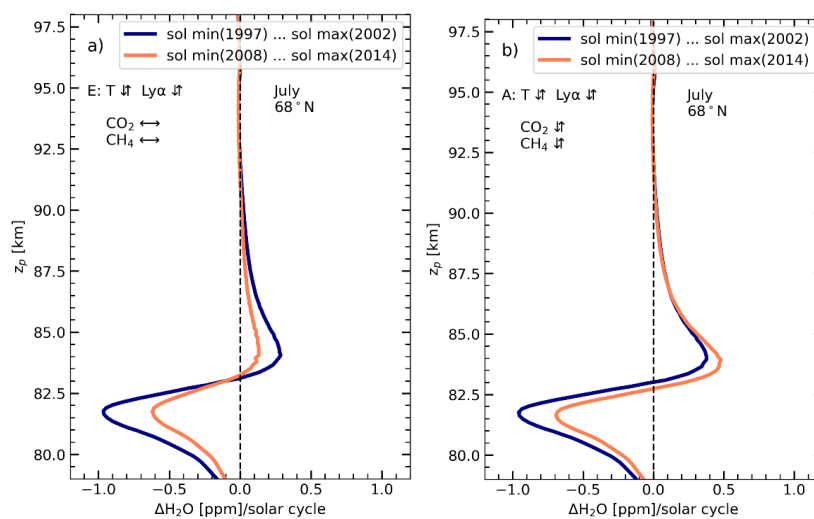
636

637



638 Figure 7. H₂O-response to absolute solar cycle Ly α variations in July at 68°N during the years
639 between solar minimum and maximum in the early (1997 to 2002) and late (2008 to 2014)
640 periods. (a) MIMAS model run E with constant CO₂ and CH₄, (b) MIMAS model run A with
641 varying CO₂ and CH₄.

642

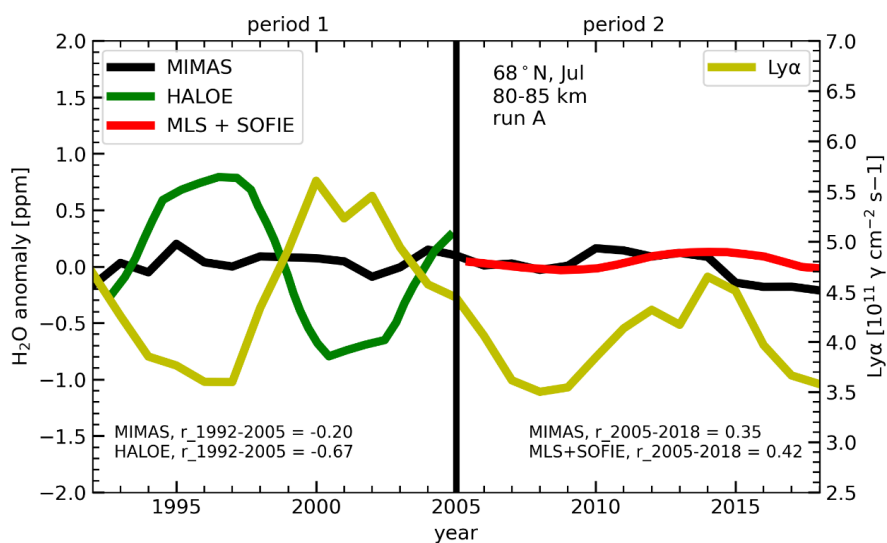


643

644



645 Figure 8. Time series of Ly α and H $_2$ O anomalies as monthly averages for July at 68°N for the
646 altitude range of 80 km to 85 km from MIMAS run A and satellites (HALOE and the composite
647 data (MLS and SOFIE)). Satellite observations are according to Hervig et al., 2019. The H $_2$ O-
648 Ly α correlation is calculated for the early and late periods (see inset).

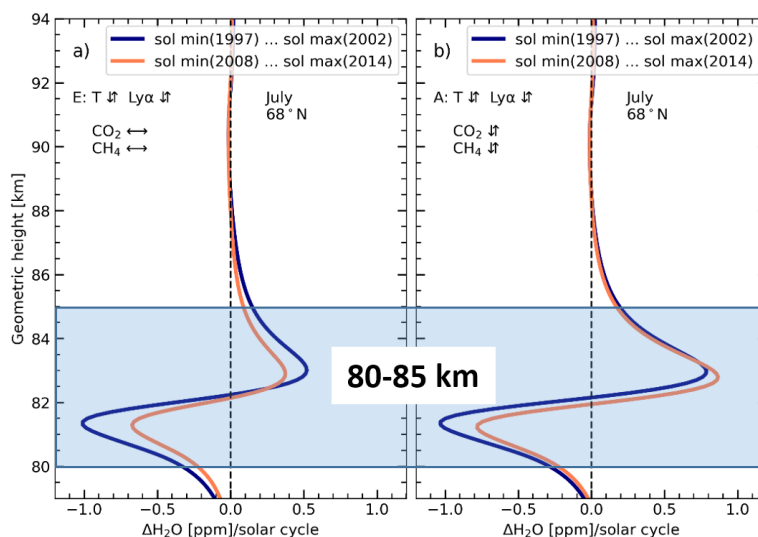


649

650



651 Figure 9. H₂O-response to absolute solar cycle Ly α variations in July at 68°N during the years
652 between solar minimum and maximum in the early (1997 to 2002) and late (2008 to 2014)
653 periods represented in geometric altitudes. The shaded region represents the altitudes range
654 used for calculating an average solar cycle response. (a) MIMAS model run E with constant
655 CO₂ and CH₄, (b) MIMAS model run A varying CO₂ and CH₄.



656
657
658
659
660
661
662
663
664
665
666
667
668
669



670 **Tables**

671 Table 1. MIMAS simulations were carried out under different background conditions. The
 672 horizontal arrow stands for constant values for the given year; the vertical arrow is for varying
 673 parameters. How Ly α affects H₂O is given for each run in the last column.

674

	LIMA		MIMAS		
Model run	CO ₂	Ly α T effect	CH ₄	Ly α photolysis effect	Water vapour solar cycle response affected by
A	↓	↓	↓	↓	<ul style="list-style-type: none"> • Temperature change (Lyα + CO₂) • Photo dissociation • Varying CH₄ (H₂O source)
E	↔ 1997	↓	↔ 1997	↓	<ul style="list-style-type: none"> • Temperature change • Photo dissociation
F	↔ 1997	↓	↔ 1997	↔ 1997	<ul style="list-style-type: none"> • Temperature change
G	↔ 1997	↔ 1997	↔ 1997	↓	<ul style="list-style-type: none"> • Photo dissociation

675

676

677

678

679



680 Table 2. The solar cycle H₂O response averaged over 80-85 km geometric altitude at 68°N
681 for model runs A and E.
682

Model run	$\Delta\text{H}_2\text{O}$ (ppm)/solar cycle (80-85km)	
	Early period	Late period
MIMAS with constant CO ₂ and CH ₄ (run E)	-0.11	-0.06
MIMAS with increasing CO ₂ and CH ₄ (run A)	-0.01	0.10

683
684
685
686